Imaging Co-Seismic Fault Zone Deformation from Air Photos: the Kickapoo Stepover along the Surface Ruptures of the 1992 Landers Earthquake.

Rémi Michel (1) and Jean-Philippe Avouac (2)

(1) Laboratoire de Détection et de Géophysique, CEA, BP 12, Bruyères-le-Châtel Cedex, 91680, France. remi.michel@cea.fr

(2) Tectonics Observatory, Geological and Planetary Sciences, California Institute of Technology, Mail code 100-23, PASADENA, CA 91125 USA.

avouac@gps.caltech.edu

Abstract.

Co-seismic deformation of the ground can be measured from aerial views taken before and after an earthquake. As a test example we chose the area of the Kickapoo-Landers stepover along the 1992 Landers earthquake zone, using air photos in a scale of 1:40,000 scanned at 0.4 m in resolution. A pair of photos acquired after the earthquake is used to assess the accuracy and evaluate various sources of noise. Optical distortions, deformation of films, scanning errors or errors on viewing parameters can yield metric bias at spatial frequencies lower than 1km-1. Offset field at shorter wavelength is more reliable and mainly affected by temporal decorrelation. This factor and resulting uncertainty on offsets are assessed from correlation score. Surface relative displacements are measured with independent measurements every about 15 m and an uncertainty typically below 10cm (rms). The offset field reveals most of the surface ruptures mapped in the field, and the fault slip is measured with accuracy of about 7cm (rms) and independent measurement every 200 m from stacked profiles. Slip distribution compare well with field measurements at the kilometric scale but reveal local metric discrepancies suggesting that deformation is generally, though not systematically, localized on the major fault zone measured in the field. This type of data can provide useful insight on fault zone's mechanical properties. Our measurements indicate that elastic co-seismic strain in the near fault zone can be as large as 0.5 10^{-3}, while anelastic yielding was attained for strain in excess of about 1-2 10^{-3}.

1. Introduction

Earthquake ruptures can form a sharp, knife-edge, fault trace or a rather broad shear zone which can be a few 100m to a few kilometers wide. The geometry of these surface ruptures and the measurement of the ground deformation are key observations to investigate the mechanics earthquakes and faults zone's constitutive properties [e.g., Fialko, 2004]. First the measurement of surface fault trace and slip distribution are a primary source of information on the fault geometry and co-seismic slip distribution at depth. Combined to seismological observations, these data provide boundaries conditions helpful to constrain the kinematics of seismic rupture. Finally fault geometry and associated slip distribution might be a key factor determining dynamic rupture, the conditions for propagation or arrest of the seismic rupture, and the frequency content of the radiated seismic waves [e.g. Hernandez et al., 1999]. Understanding better co-seismic ground deformation is also of interest to anti-seismic engineering since a significant fraction of near-fault damages to engineering structures result from permanent ground deformation rather than from ground shaking, as was observed for example during the Chichi earthquake. Measuring co-seismic deformation in the near fault zone is therefore a major issue in seismotectonics. However, this piece of information is not always easy to gather and there is a therefore a need for methodological improvements.

Hereafter, we first discuss the limitation of field investigations and the potential of remote sensing techniques. We next show that these measurements can be made from correlation of air photos taken before and after co-seismic deformation. We chose a test case that has received much attention already, the Kickapoo step-over along the fault trace of the 1992, Mw 7.3, Landers earthquake [Spotila and Sieh, 1995; Johnson et al, 1994; Sowers et al, 1994; Peltzer et al, 1994] making it possible to compare our measurements with detailed field observations. The primary objective of this analysis is to assess the potential and limitations of the technique and identify the main source of uncertainties.

2. Measuring fault zone deformation from field investigations and remote sensing technique.

Geometry of fault ruptures and coseismic slip are generally determined from investigations in the field. While surface fractures are relatively easy to detect and map, it is not always easy to measure accurately offsets across the fault zone. The measurement of the offset parallel to the fault trace (including the strike-slip and vertical components) can generally be made only at a limited number of sites where natural or anthropogenic features which used to be continuous across the fault zone, have been clearly offset by a measurable amount [Yeats et al., 1997; Weldon et al., 1996]. Even in a favorable case, the uncertainty on the geometry of feature before co-seismic deformation leads to considerable uncertainty on the measurement of co-seismic displacement across the fault zone. The component of displacement perpendicular to the fault is generally not measurable directly, and is generally inferred from the vertical component of fault displacement assuming some fault dip angle. In the case where the seismic ruptures have a complex geometry or form a broad zone of distributed faulting, estimating the total slip across the fault zone is even more difficult. In addition, the zone of co-seismic anelastic strain might be significantly broader than the zone where ruptures are clearly seen at the surface [*e.g.,* McGill, S.F. and Rubin, 1999, Simons et al, 2002; Binet and Bollinger, 2005]. In the case of the Landers earthquake (Figure 1), surface fault slip was measured in the field at a considerable number of points [e.g., Sieh et al, 1993, Sowers et al, 1994]. The total slip across the fault zone, estimated by adding offsets measured on the various ruptures recognized in the field, show significant lateral variations. It is unclear whether this variability reflects near surface complexities of deformation or slip variability on the seismic fault at depth. Indeed it has been observed that co-seismic ground shear was distributed at some places in a zone possibly as broad as 1-2 km and may amount to as much as 20% of the total slip across the fault zone [e.g., Johnson et al, 1994; McGill and Rubin, 1999; Yeats et al., 1997].

Imaging ground deformation in the fault zone using remote sensing techniques should allow overcome some of the limitations of field measurements. Various techniques based on satellite imagery might be used. Differential SAR interferometry is a powerful technique to measure co-seismic ground deformation [Massonnet et al., 1993; Zebker et al., 1994] but it generally fails in the near-fault zone where large displacements result in poorly correlated images and eventually signal decorrelation [Michel et al., 1999; Simons et al, 2002]. The use of sub-pixel correlation of SAR amplitude images can partially supplement this technique as it provides an unambiguous measurement of both the track-parallel and track-perpendicular components of the ground displacement [Michel et al., 1999; Peltzer et al., 1999; Simons et al, 2002; Fialko, 2004]. The use of optical satellite imagery is an alternative technique [Crippen, 1992; Van Puymbroeck et al., 2000; Michel and Avouac, 2003; Dominguez et al, 2003; Binet and Bollinger, 2005]. It suffers from some technical limitations regarding the spatial resolution and long wavelength bias induced by the changing attitude of the satellite, but it has proved to be a quite robust technique. As an example, we show the NS offsets due to the Landers earthquake measured from a pair of SPOT images with 10 meter ground resolution (Figures 2 and 3). This technique is promising for the analysis of future events, especially with the development of higher resolution satellite imagery and an improved control of the satellite attitude (for example using very high resolution SPOT-5 imagery [Binet and Bollinger, 2004]). Only a limited number of past earthquakes can be analyzed from this approach due to the lack of available very high resolution satellite images. In the next section we show that air photos can be used in very much the same way, offering a better spatial resolution and accuracy in the near fault zone than has been achieved with satellite imagery and the possibility to take advantage of existing archives on a number of past large earthquakes.

3. Study area: the Kickapoo stepover along the Landers EQ fault trace.

In 1992, the Mw 7.3 Landers earthquake ruptured portions of four preexisting main faults: the Johnson Valley, the Homestead Valley, Emerson and Camp rock faults [*e.g.*, Sieh et al, 1993]. Probably due to the non-optimal orientations of these faults with respect to the pre-seismic tectonic stress field, the earthquake only ruptured favorably oriented fault segments, resulting in a complex fault geometry with a number of jogs [Bouchon et al, 1998] (Figure 1). The Kickapoo stepover is one of these major jogs (Figure 4). The Johnson Valley Fault (JVF) bends gradually from N15E to N30E south of the stepover to N30E north of it. As the fault bends, becoming more and more orthogonal to the maximum direction of horizontal stress [Hardebeck and Hauksson, 2001], slip on JVF tapers from nearly 5 meters south of the step-over to zero over a distance of a few kilometers. North of the Step over slip along the Homestead Valley Fault (HVF) is of the order of 3 meters. The Landers Kickapoo fault (LKF), which strikes about N-S and is therefore nearly optimally oriented with respect to the tectonic stress field, is the main zone of deformation connecting JVF and HVF. It consists of 50-100m wide shear zone with dense fracturing. InSAR measurements [Peltzer et al, 1994] reveals that the domain west of LKF was tilted southwards by an amount consistent with the gradient of vertical slip measured in field along LKF [Spotila and Sieh, 1995]. The area where KVF joints with HVF has been recognized as a zone of complex and distributed deformation, with dominantly thrust faulting, and has been inferred to correspond to a major slip gap with possible bearing on the rupture dynamics process [Spotila and Sieh, 1995]. The joined inversion of SAR and GPS data suggest 1-2m of shallow slip (at depth less than 5km) and some slip gap at depths between 3 and 10km (Figure 9 in [Fialko, 2004]). The joined inversion of seismological and geodetic data indicates that the rupture front was decelerating when rupturing zones of reduced slip, in particular around the Kickapoo stepover, and accelerating when rupturing slip asperities [Hernandez et al., 1999]. In figure 3 we show several profiles in the offset field measured from the SPOT images run across the fault zone in the Kickapoo stepover aera. These profiles suggest that the total slip across the fault zone is 3.5 +-0.5 m south of the stepover, a value consistent with field measurements, and decreases to about 2.0+-0.5 m just north of the stepover in the slip gap zone of Spotila and Sieh [1995]. So the SPOT offsets field suggests a non-null strike-slip offset but the detailed of the slip distribution and fault rupture is poorly constrained from these measurements.

4. Data and Method.

We have acquired air photos covering the Kickapoo stepover and determined surface displacements form sub-pixel correlation of images acquired before and after an earthquake (Figure 5). Two images acquired after the Landers earthquakes were used to estimate errors and potential bias associate with this technique. As described below, the procedure requires digitization, geo-coding and cross-correlation of the images.

4.1 Data

The data used in the present study are listed in Table 1. We have used film negative from the US National Aerial Photography Program (NAPP) aerial images. The images are acquired in a 5-7 years cycle, aircraft altitude is 20.000 feet, the focal length is 6 inches, images are 9 by 9 inches in size covering an area of slightly more than 5 miles on a side. Nominal roll, pitch and yaw are zero. Due to the effective geometric and photometric quality of the data the effective ground resolution is about 1 m [USGS, 1992] while the film nominal resolution is about 10 µm corresponding to 0.4m on the ground [Kodak, 2003]. We used one image acquired on 25-07-1989 before the June, 1992 Landers earthquake, and two images acquired after the earthquake (on 10-03-1995, and 01-06-2002). Variations in sun illumination and ground radiometry (including man made and natural evolutions of the scene) yield temporal decorrelation of the images (figure 5). In order to produced orthorectified, geocoded images we used the 1 arc sec US National Elevation Data Set [Osborn et al., 2001]. Expected vertical accuracy is about 10 meters (rms).

4.2 Processing flow chart

1-Digitization.

The images were digitized with a micro-densitometer nominally designed for astronomical applications (*e.g.* cartography of stellar objects magnitude) [Guibert and Moreau, 1991]. It consists of a 1024 pixels photodiode array which sensitivity is centered at 633 nm. Geometrical quality of this instrument mainly relies on Heidenhain optical ruler with an accuracy of 0.1 µm. Resulting accuracy (i.e. the standard deviation of the instrumental gaussian white noise on the location of pixels) and repetitiveness (i.e. the systematic error) on the scanned images are respectively 0.6 and 0.2 µm. Photometry quality results in 12 bites images digitization. This digitization is a reduction of the dynamic of analogical films but is still over dimensioned for our set of images suffering temporal radiometric decorrelation. The very good quality of Modulation Transfer Function (MTF) of the microdensitometer (Figure 6) is well suited for this application because it is compatible with the resolution of the films and thus allows to correlate high frequency features and minimizes the aliasing that has been demonstrated a source of noise on correlation maps [e.g. Binet and Bollinger, 2004].

2-Geocoding

Geocoding is performed following a tree steps procedure. First, a raw geocoded image is performed at the resolution of the DEM (3arcsec) using the geometrical parameters provided with the images. This image is then correlated with either a shaded DEM computed with the appropriate scene illumination, based on the sun position at the time of acquisition of the image. An alternative approach would be to use a reference geocoded image such as a SPOT orthoimage. The correlation is computed from

Symmetrical Phase Only Filter method [Michel et al., 1999a]. This procedure yields a set of ground control points (GCP) with associated uncertainties on the measurement of their co-registration. These GCPs are then used to estimate the parameters of the air photos: Roll, Pitch, Yaw, scene center coordinates, aircraft altitude, focal length. For that determination we use an iterative least squares procedure. Once these parameters are obtained, the image is geocoded in UTM, WGS84 at 0.4 meter resolution using a “sinc" resampling kernel 11x11 pixels in size [Van Puymbroeck et al., 2000]. The typical number of GCP is several hundreds and the standard deviation between the GCP positions in the DEM and in the geocoded image, after optimization of the acquisition parameters, is 2.1 m in average.

3-Sub-pixel correlation

We have adapted the correlation technique of Van Puymbroeck et al. [2000] which was initially designed for correlation of SPOT images. Offsets are computed from the phase shift of the Fourier transform of a sliding window n x n pixels in size. If the two components of offsets do not exceed $n/4$, it provides a measure of the two horizontal components of the ground displacement with an estimate of the uncertainty associated with the quality of the correlation. With SPOT 10-m resolution images offsets due to co-seismic deformation range most generally within 1 or 2 pixels because co-seismic ground displacements rarely exceed 10 meters. On air photos offsets may exceed 10 pixels so that the technique needed to be adjusted.

We used a multi-scale procedure. Experience shows us that n=32 is an optimal value to correlate natural scenes. Images are resampled by a decreasing factor equal to 8, 4, 2 and 1. Offsets are computed at each step and values of low coherence suggesting errors on offsets greater than 0.5 pixels (figure 9) are replaced by local polynomial interpolation. For a given resampling factor, the offsets computed at the previous step are used to center the correlation windows in order to measure offsets below the critical *n/4* value. An nearly equivalent approach, consists in using decreasing values of *n*, merely yields the same final result.

The calibration procedure described in Van Puymbroeck et al. [2000] is still adapted to this procedure. It yields the correction of residual systematic correlation errors that may result from residual aliasing and temporal decorrelation (both sources yield underestimates of the sub-pixel amplitude of offsets). The calibration function is computed as the difference between theoretical and measured sub-pixels values. For that purpose, images are artificially shifted by sub-pixel quantities in the range [0,1] using a sinc kernel and white gaussian noise of various standard deviation are added to simulated different rates of temporal decorrelation [Van Puymbroeck et al., 2000]. The offsets fields computed in this study have been obtained with a final 32x32 correlation window and a step of 16 pixels. Note that, due to the multi-scale procedure, adjacent measurements are not totally independent since they incorporate information obtained from correlating overlapping windows. The procedure thus provides independent measurements every about 15 m on the ground.

5. Estimation of errors and bias.

The procedure was first applied to the two images that were both acquired after the Landers earthquake so that the actual ground displacement field should be null (Figure 7a and b). We have measured the apparent offsets between the two images in order to assess the accuracy and potential bias of our procedure. The distribution of measured offsets is centered on zero and is nearly Gaussian with a standard deviation of 0.65

pixels or 26 cm (Figure 7c). This yield an empirical estimate of the cumulative effect of all sources of error. This statistical description of errors is however somewhat misleading because, as it has also been shown for SPOT images [Vanpuymbroeck et al., 2000], the distribution of errors highly depends on the spatial wavelength and errors can thus not considered a Gaussian white noise (Figure 7d). Figures 7b and c show the high pass offsets map filtered out of wavelength lower than $1km^{-1}$. They indicate that offsets measured below the kilometric scale include noise with a standard deviation as low as 0.18 pixel or 7.2 cm. Frequencies below $1km^{-1}$ were fitted by an order 3 polynomial with min max values as large as 2.0 m.

At this step we can conclude that aerial images will provide useful information about earthquake's induced displacements below the kilometric scale.

1- Optical Distortions

Residual optical distortions of the camera and the thermal image beam deflection near the aircraft result in geometrical distortions of few micrometers on the films [*e.g.* Schöler, 1975]. No calibration is available to compensate for these distortions. They moreover are not automatically compensated during the correlation procedure because they depend on the field (and on the optical aperture) and thus vary within an image and because differences in scene centers and flight directions induce varying locations of the images of a given point on the ground. Moreover, these distortions are wavelength dependant, (they increase by a factor of two on average from blue to red [Schöler, 1975]) and thus can not be recovered from panchromatic images. This optical distortion results in low frequency bias on measured offset with a typical magnitude of only a few tenths of centimeters on the ground.

2- Film's deformation

Negative films suffer temporary and permanent thermo-mechanical deformations that mainly depend on temperature, relative humidity and age [*e.g.* Kodak, 2003; Agfa, 2000]. These deformations are primarily isotropic locally but might not be homogeneous. State of the art aerial films are known to suffer temporary deformations of about 20µm per meter per Kelvin and 20µm per meter per percentage of relative humidity. Permanent changes include deformations of about 0.025% resulting from processing and an aging shrinkage of a few hundredths of per cent per month for standard storage conditions [Kodak, 2003]. The microdensitometer's room is controlled to 20+-1°C and about 0.5% in relative humidity and the films were scan few months after processing. We can thus assume a dimensional stability typically worse than few tens of µm for our 9 inches films. This term is partly corrected when the viewing parameters are adjusted so that deformation of the print is misinterpreted for a difference of focal position, viewing angles, and focal lengths. A large residual error may remain as shown form our test example. Thus, film distortions result in irremediable low frequency bias with magnitude greater than 1m on the ground and thus put severe limitations on the accuracy of the measured offsets at long wavelength. It is a major importance for our study to note that no information is available from the opened literature about the geometry of the film's deformation. One way to limit this source of noise would be to scan original glass plates. For glass plates, thermo-mechanical deformations are estimated to be less than about 5 µm/m/K and the response to relative humidity is negligible [Ligterink, 1971, USGS].

3- Scanning errors

The geometric stability of the densitometer is such that scanning errors at the scale of the negative should not exceed 1 µm (see § 4.2 digitization) leading to errors in the offset field of less than about 4 cm on the ground. A line orientated bias pattern of this amplitude has been detected on the images (Figure 7b). This pattern should result from the errors on repetitivity during the line by line scanning procedure. Measured resulting error is however 5 time greater than the specified 0.2 µm error in repetitivity (see § 4.2). The wavelength on the ground corresponding to this scanning artifact is about 100m and is post-compensated on offset maps by assuming line by line invariance of averaged offsets.

4- Uncertainty on viewing parameters.

The geocoding procedure implies that the images are all tied to a set of GCPs which are assumed fixed. In the case of SPOT images the GCPs can be chosen in the far field where co-seismic displacements are small. This is not the case with the air photos. It result that the offsets at the GCP are partly compensated when the viewing parameters of the images are adjusted. These adjustments are generally smaller than the uncertainties on the viewing parameters. The long wavelength in the offsets field are then misinterpreted as resulting from erroneous viewing parameters and are forced to be null on average for the selected set of GCPs. In order to illustrate that point, we have computed a theoretical model of ground displacement in the study area using the model proposed by Hudnut et al.[1993] (Figure 8a). We have next computed the adjusted viewing angles that would minimize the misfits between the observed and predicted position of the GCPs, assumed fixed, for two images that would be acquired before and after the earthquake. Figure 8b is showing the long wavelength offset field that is then misinterpreted as a view angle difference rather than by ground displacement. This field can be approximated, to within few centimeters, by a degree 2 polynomial function. Indeed if we consider that the scene is a flat field, modification of viewing parameters results in changes in pixels' location describing an order 2 polynomial because of the conic projection of aerial images. During that procedure the displacement field at the GCPS is absorbed by a correction of roll, pitch and yaw by less than 0,02° and a shift of the scene center by only 1m. The corrections are smaller than the nominal uncertainties on these parameters (about 0.1°) There is therefore no hope that the long wavelength (>5km) deformation field be measured from this technique. This is an intrinsic limitation that could be overcome by measuring the GCPs simultaneously with image acquisition, or by assuming some values of ground displacements at the GCPs (based for example on some a priori model of co-seismic deformation).

5- DEM errors

Because a given point on the ground is not acquired with exactly the same viewing parameters on the two images, vertical uncertainty of the DEM results in scene dependant geometrical deformation of the geocoded images and consequently contributes to errors on offsets. This error is of the order of $\Delta z.\ \Delta i$ where $\Delta z.\ \Delta i$ are respectively the vertical error on the DEM and the maximum difference in viewing angles. For example, a difference in scene center of 100 m (observed for the images of this study) and a 10 m error in elevation (typical of the 1-sigma uncertainty on elevation in a DEM), results in an apparent, erroneous offset of about 0.2 m between the two geocoded images. Since offsets are measured within *nxn* window, one should expect the error on offsets to be divided by square-root-n. Unfortunately due to systematic errors resulting in part form the poorer spatial resolution of the DEM, the error reduction is not that much (something around 1cm for n=32). Errors on measurements of offsets due to the DEM errors will be correlated with the DEM and will be typically be smaller than a few centimers in the present study for correlation window of 32x32 in size . The use of a SRTM DEM would yield about the same accuracy..

6- Decorrelation

Images of natural scenes acquired at different dates suffer temporal decorrelation mainly resulting from changes in surface radiometry, in atmospheric and enlightenment conditions and in viewing and detection parameters.

Most rates of temporal decorrelation increase with the spatial frequency because landscape generally varies more rapidly at high spatial frequencies than at low frequencies. We can thus foresee a greater rate of temporal decorrelation per pixel for metric or submetric imagery than for SPOT decametric imagery. The contribution of the temporal decorrelation to the uncertainty on the measured offsets can be estimated from the local correlation score [Vanpuymbroeck et al., 2000] (Figure 9). This score does not provide information about the prominent low frequency (spatial frequency lower than *1/n* pixel^{-1}, where *n* is the size of the correlation window) sources of noise and bias on offsets listed above.

In this study the correlation score is used as a weighting factor during the stacking procedure of profiles on offsets across the ruptured fault zone (Figure 11, 12, 13).

Measured correlation score is 0.61 in average corresponding to decorrelation on offset equal to 0.23 pixel in average or about 10 cm in the ground.

6. Measurement of co-seismic deformation in the Kickapoo stepover area.

In this section, we show that in spite of the limitations listed above, we were able to detect ground deformation in the Kickapoo stepover area from correlating air photos taken before and after the Landers earthquake. The offsets field allows mapping fault ruptures and measuring fault-slip with accuracy and a spatial resolution comparable to what can be achieved from field measurements.

Results obtained from applying the procedure described below to the images of the Kickapoo stepover acquired before and after he Landers earthquake are shown in figure 10. Discontinuities in the measured NS and WE offset field clearly show up and correlate with the fault ruptures mapped in the field [Spotila and Sieh, 1995] (Figure 4). At high frequency (for wavelengths less than about 1km) the noise level estimated from the correlation score is about 21cm at the 3-sigma confidence level. Distortions at longer wavelength are about 4 meters in amplitude. These distortions do not affect the determination of the fault geometry, nor the possibility of measuring the fault slip across the fault zone.

The horizontal component of fault slip was determined from profiles run perpendicular to the fault trace. In figure 11 we have reported such profiles that were stacked along 1-2 km long fault segments. Due to the slightly sinuous fault geometry the stacked profiles might be taken to suggest a shear zone with finite width. Closer inspection of the offsets field reveals that the high strain zone corresponding to the fault ruptures is actually very narrow, typically less than 50m in general, except in the seismic gap zone (indicated in Figure 4). It might be even less in reality but a narrower width cannot be resolved given the size of the correlation window (32x32). These profiles clearly indicate that these faults are purely strike-slip except for the Homestead valley fault segment north of junction with the Landers- Kickapoo fault, which is a pure thrust fault (profiles 7 and 8 in Figure 11). The fault slip was measured by fitting 0.6km long profiles across the fault as the sum of a step-function and a linear term. In figure 12 we report these measurements made every 200 m by stacking the profiles within each 200m wide swath. The uncertainty on fault slip (defined as the amplitude of the step-function) was estimated from the rms of the fit to each profile. Our measurements agree remarkably well with the field measurements of Spotila and Sieh [1995] along the JVF, the LKF and the Southern segment of the Homestead Valley fault (SHVF). The main discrepancy is along the northern end of the LKF where the ground ruptures get more complicated at the junction with Homestead Valley Fault.

Although the fractures were identified and mapped in the field, no measurements of he fault slip could be done along the secondary fault zone which parallels LKF corresponding to profile 9 in Figures 4 and 11. The profile run in the air photos offsets reveal 20+/-7cm of strike-slip displacement across that feature on average (Figure 11). This example shows that relatively subtle features, not easily measurable in the field, can be identified and measured from Air photos offsets.

Figure 12 shows a stack of all profiles within a 2 km wide swath across the surface slip gap zone (see location in Figure 4). This profile suggests indicates that there is no localized shear zone, but rather a relatively diffuse shear zone about 1km wide. It is however unfortunately located in an area of large low spatial frequency artefact (Figure 10) so that elastic modelling of slip at depth can not be carried out. This shear zone corresponds closely with distributed ground ruptures observed in the field [Spotila and Sieh, 1995] (Figure 4). The displacement across each of these individual fractures, which are too small to show up in the air photos offsets, could not be measured in the field. The air photos offsets show that the total slip across the shear zone is between 2 and 3m. The uncertainty on this measurement cannot be easily estimated because of the various possible geometric distortions at long wavelength listed in the previous section. This measurement is consistent with the 2.5m slip measured from the SPOT offsets (Figure 3), and with the 1-2m shallow slip patch inferred from SAR images [Fialko, 2004].

7. Some seismotectonic implications

1- Fault geometry, Localized fault slip vs distributed anelastic shear.

The offset field reveals the geometry of the faults which ruptured during the Landers earthquake. The Landers-Kickapoo fault shows a sinuous pattern with a typical wavelength of 1km which we interpret to reflect en-echelon faults that coalesced to form the presently. Geomorphic discontinuity observed on the pre-Landers earthquake image suggest that this fault existed already before that earthquake, but it is clearly a young feature and the sinuosity might be reminiscent of en echelon Riedel shears which first formed across the step-over. By contrast the Johnson valley fault is much more linear, as expected for a fault with more cumulative slip. Indeed faults tend to straighten and become more continuous as cumulative slip increases [Wesnousky, 1988].

The consistency between the measurements of fault-slip measured in the field and from the Air Photos offset show that, once a localized fault is formed very little deformation is absorbed off the main fault trace. Field measurements might however be affected by some variability at small scales not captured by the Air Photos offsets. In that case the field measurements might significantly underestimate the total slip but we believe, based in this example that this generally does not occur when a major fault trace clearly dominates the fault pattern. This means that field measurements of slip (associated either with a recent or a paleoseismic events) along a well expressed major fault trace are probably generally representative of the total slip across the fault zone. The fact that we reach this conclusion in a zone where the fault geometry is relatively complex implies that strain localization on a single fault does probably not require much cumulative slip. Given that the cumulative slip on JVF and SHVF is of the order of only about 300m, and that cumulative slip on LKF must be significantly less [Spotila and Sieh, 1995], a cumulative displacement of 100 meters might be sufficient for strain to localize on a major fault.

Our measurements confirm that the portion of Homestead Valley fault north of the intersection with LKF is a zone of relatively lower fault slip, as proposed by Sieh et al [1992] and Spotila and Sieh [1995]. The fact that no well localized fault zone was able to form there is probably due to the fact that the intersection between the LKV and the SHV strike-slip faults cannot be stable. Cumulative deformation has induced bending of the Homestead Valley fault and distributed deformation in the area surrounding the faults junction. In this case, although cumulative slip is large, the instability of the junction has prevented the formation of a localized fault zone.

We conclude that once a stable fault zone geometry is attained the development of well localized fault zone probably requires less than few 100m cumulative slip.

2-Implication for the determination of the critical strain before anelastic failure.

Our measurements of surface strain produced by the Landers earthquake yield information on the critical strain which can be sustained elastically by near surface rocks. Lateral variation of slip along the JV, SHV and LK faults implies co-seismic fault-parallel elongation or contraction of the surrounding medium of the order of 0.5 10^{-3} (typically 0.5m/1km) (Figure 12). The best constraints come from the gradual northward tapering of slip along the JVF. This deformation must be primarily elastic since field investigations didn't reveal any evidence for fracturing that would have resulted from this strain [Spotila and Sieh, 1995; Sowers et al, 1994]. Profiles run perpendicular to the fault also indicate typical value of shear strain of the same order of magnitude (Figure 11). We conclude that that the near surface rocks in the Landers area could sustain strain as large as 0.5 10^{-3} without visible fracturing, placing a lower bound on the limit for anelastic yielding.

On the other end, surface strain in the 'surface slip gap' area provides an idea of an upper bound. Our measurements indicate that the fault parallel displacement is of the order of 2 meters (Figure 13). This deformation is not localized on a single fault but rather distributed within a 1-km wide shear zone, within which the strain is about 2 10^{-3}. Fractures were observed in the field within this shear zone suggest that this strain is in excess but probably close to the maximum elastic strain sustainable by near surface rocks. This estimate is in agreement with rock mechanics experiments carried on initially intact westerly granite which suggest that, at confining pressure of less than about 50MPa (corresponding to depths shallower than 2km), the critical strain for fault strain localization would be of the order of 1-2 10^{-3} [Lockner, 1998].

We therefore conclude that, during co-seismic deformation, the critical strain for anelastic yielding of surface rocks in the Landers area is of the order of 1 10^{-3}, and that anelastic strain in excess of about 1-2 10^{-3} is necessary for strain localization and hence strain drop. We might speculate that the propagation of the rupture front across the slip gap area was a sink of energy, as suggested by the decrease in rupture velocity [Wald and Heaton, 1994; Hernandez et al, 1999], because the critical strain localization, which is required for significant stress drop [Lockner, 1998], was not attained.

8. Conclusion

This study shows that near-field co-seismic ground deformation can be measured in some detail using air photos using a correlation technique analogue to that developed for satellite imagery in earlier studies [Michel et al, 1999; Van Puymbroeck et al, 2000]. This approach is a useful complement to other remote sensing techniques, such as SAR interferometry, or field investigations. Limitations of the technique are essentially due to possible deformation of the analogue support and inaccurate knowledge of the image parameters (position, elevation of the plane). The development of new survey techniques for digital Air Photos acquisition in which the plane position is determined from Real Time Kinematics GPS will help overcome these problems. In spite of these limitations the technique can be used to map fault ruptures to within a few tens of meters and measure fault slip with a accuracy of about 10-20cm (with an sampling rate of a few points per kilometers). This kind of measurements can provide useful insight on fault zone mechanical properties.

References

Agfa-Gevaert, Panchromatic negative film for aerial photography, aviphot pan 400s PE 1, B2640 Mortsel-Belgium, october 2002.

Binet, R., and L. Bollinger, Horizontal coseismic deformation of the 2003 Bam (Iran) earthquake measured from SPOT-5 THR satellite imagery, *Geophysical Research Letters*, *32*, 10.1029/2004GL021897, 2005.

Bouchon, M., M. Campillo, and F. Cotton, Stress field associated with the rupture of the 1992 Landers, California, earthquake and its implications concerning the fault strength at the onset of the earthquake, *Journal of Geophysical Research-Solid Earth*, *103* (B9), 21091-21097, 1998.

Dominguez, S., J.P. Avouac, and R. Michel, Horizontal co-seismic deformation of the 1999 Chi-Chi earthquake measured from SPOT satellite images: implications for the seismic cycle along the western foothills of Central Taiwan, *J. Geophys. Res.*, *108*, 10.1029/2001JB000951, 2003.

Fialko, Y., Probing the mechanical properties of seismically active crust with space geodesy: Study of the coseismic deformation due to the 1992 M(w)7.3 Landers (southern California) earthquake, *Journal of Geophysical Research-Solid Earth*, *109* (B3), 000220624100002 , 2004.

Guibert, J. O. Moreau, Photographic Astronomy with MAMA, The Messenger, 64, p. 69-70, 1991.

Hardebeck, J.L., and E. Hauksson, Crustal stress field in southern California and its implications for fault mechanics, *Journal of Geophysical Research-Solid Earth*, *106* (B10), 21859-21882, 2001.

Hernandez, B., F. Cotton, and M. Campillo, Contribution of radar interferometry to a two-step inversion of the kinematic process of the 1992 Landers earthquake, *Journal of Geophysical Research-Solid Earth*, *104* (B6), 13083-13099, 1999.

Johnson et al, BSSA 1994.

KODAK aerochrome HS Film SO-359, Publication N° AS-207, 2003.

Kraus, Karl Photogrammetry, Fundamentals and Standard Processes 1993, Dümmlers Ligterink, G.H., Film-Glass Differences, International Symposium on Image Deformation, Ottawa, Canada, 269-273, 1971.

McGill, S.F. and Rubin, C.M. Superficial slip distribution on the central Emerson fault during the June 28, 1992, Landers earthquake, California, *J. Geophys. R.*, 104, B3, 4811–4833, 1999.

Liu, J., K. Sieh, and E. Hauksson, A structural interpretation of the aftershock "Cloud" of the 1992 M-w 7.3 Landers earthquake, *Bulletin of the Seismological Society of America*, *93* (3), 1333-1344, 2003.

Lockner, D.A., A generalized law for brittle deformation of Westerly granite, *J. Geophys. Res.*, *103*, 5107- 5123.

Michel, R., J.P. Avouac and J. Taboury, Measuring ground displacements from SAR amplitude images : application to the Landers earthquake, *Geophys. Res. Lett.* , 26, 875-878, 1999.

Michel, R., Avouac, J.P. and Taboury, J., Measuring near field coseismic displacements from SAR images : application to the Landers earthquake, *Geophys. Res. Lett*., 26, 19, 3017–3020, 1999.

Osborn, K., List, J., Gesch, D., Crowe, J., Merrill, G., Constance, E., Mauck, J., Lund, C., Caruso, V., and J. Kosovich. Chapter 4 – National digital elevation program (NDEP), in Maune, D., ed., Digital Elevation Model Technologies and Applications:

The DEM Users Manual: Bethesda, Maryland, American Society for Photogrammetry and Remote Sensing, p. 83-120, 2001.

Paine, David P., Aerial Photography and Image Interpretation for Resource Management, John Wiley & Sons, 1981.

Peltzer, G., K.W. Hudnut, and K.L. Feigl, Analysis of Coseismic Surface Displacement Gradients Using Radar Interferometry - New Insights into the Landers Earthquake, *Journal of Geophysical Research-Solid Earth*, *99* (B11), 21971-21981, 1994.

Sieh, K., L. Jones, E. Hauksson, K. Hudnut, D. Eberhartphillips, T. Heaton, S. Hough, K. Hutton, H. Kanamori, A. Lilje, S. Lindvall, S.F. McGill, J. Mori, C. Rubin, J.A. Spotila, J. Stock, H.K. Thio, J. Treiman, B. Wernicke, and J. Zachariasen, Near-Field Investigations of the Landers Earthquake Sequence, April to July 1992, *Science*, *260* (5105), 171-176, 1993.

Scherz, J. P., Errors in Photogrammetry. Photogrammetric Engineering 40 (4):493-500, 1974.

Scholer, H. On Photogrammetric Distortion. Photogrammetric Engineering and Remote sensing 41(6):761-769, 1975.

Spotila, J., A and K. Sieh,, Geologic investigation of a “slip gap” in the superficial ruptures of the 1992 Landers earthquake, southern California, *J. Geophys. R*., 100, 543–559, 1995.

Thompson, M., Eller, R., Radionski, W., Speert, J., Manual of Photogrammetry, BookThird Edition, American Society of Photogrammetry, 1966.

U.S. Geological Survey, The National Aerial Photography Program (NAPP), factsheet: Reston, Virginia, U.S. Geological Survey, 1 p., 1992.

Van Puymbroeck, N., Michel, R., Binet, R., Avouac, J.P. and Taboury, J. Measuring earthquakes from optical satellite images, *Applied Optics Information Processing*, 39, 23, 3486–3494, 2000.

Wesnousky, S.G., Seismological and Structural Evolution of Strike-Slip Faults, *Nature*, *335* (6188), 340-342, 1988.

Zachariasen, J. and K. Sieh, The transfer of slip between two en echelon strike-slip faults: a case study from the 1992 Landers earthquake, southern California, *J. Geophys. R.*, 100, B8, 281–301, 1995.

Table and Figures

Figure 1: Map of surface ruptures induced by the 1992 Mw 7.3 earthquake after Sieh et al, [1993] with aftershocks from Liu et al, BSSA, 2004.

Figure 2: NS offset measured from cross correlation of SPOT 4 images from 27/07/1991 and 25/07/1992 [Van Puymbroeck et al, 2000]. Box shows the Kickapoo-Landers area covered by the air photos in Figure 4. Also indicated is the location of profiles shown in Figure 3.

Figure 3: Strike-parallel surface displacement measured from SPOT images correlation along profiles A, B, C and D reported in Figure 2. Note that the total apparent right-lateral offset across the slip gap area inferred from field investigations [Spotila and Sieh, 1995] is not negligible and may amount to about 2 m.

Figure 4: Mapped surface ruptures from Spotila and Sieh [1995] (dashed black lines), and ruptures derived from our interpretation of the Air Photos offsets (white lines) with location of profiles shown in Figure 11. Geocoded scanned air photo acquired before the earthquake (Table 1).

Figure 5: Post earthquake geocoded scanned air photos used in this study with close-up views at sites with particularly prominent temporal decorrelation.

Figure 6: Modulation Transfer Function of the micro-densitometer (MTF) estimated from the scan of the air photo 1 (Table 1). 10 μm resolution is achieved which is fairly compatible with resolution of negative film and minimizes aliasing. (High geometrical

and photometrical quality of microdensitometer discussed in §4.2).

Figure 7:

a) NS offsets computed from the two images acquired after the Landers earthquake (images 1 and 2 in Table 1). Correlation window 32x32.

b) image a) filtered from frequencies below $1km^{-1}$. Note E-W 100 meters wide stripes result from a scan artifact with an amplitude about 5cm.

c) Histogram of offsets field shown in a and b.

d) Spectrum of offsets showing that noise on offset maps is not white and preferentially affects low spatial frequencies.

Figure 8 :

a) Theoretical offsets in the study area computed from the model proposed by Hudnut et al.[1993].

b) Long wavelength component of the offset field which is compensated by erroneous correction of the viewing parameters. This offset field can be closely adjusted form a degree 2 polynomial function because of the near conic projection of aerial images.

Figure 9: Simulation of the effect of temporal decorrelation.

Noise on offset as a function of local correlation score. The averaged correlation score for the Landers earthquake is 0.61 corresponding to 0.23 pixel or 10 cm in the ground (rms)

Figure 10:

a) Correlation score measured for the earthquake study.

b) Composite image showing the N-S offset map (hue) and the correlation score (intensity)

c) and d) E-W and N-S offsets.

Spatial resolution is 12.8 m, independent measurement every about 15 m.

Figure 11: Strike-parallel and strike-perpendicular components of NS and EW offsets shown in Figure 10, measured along at the profiles reported in Figure 4. All profiles were run perpendicular to the local fault strike. Error bars represents the 3-sigma confidence interval determined from the correlation score (Figure 9).

Figure 12: Slip distribution along JVF, SHVF, LKF, HVF

Figure 13: Profiles across the seismic gap.

Figure 14: Cumulative-slip distribution across the fault zone.

The grey circles represent slip measured from SPOT (Figure 3).

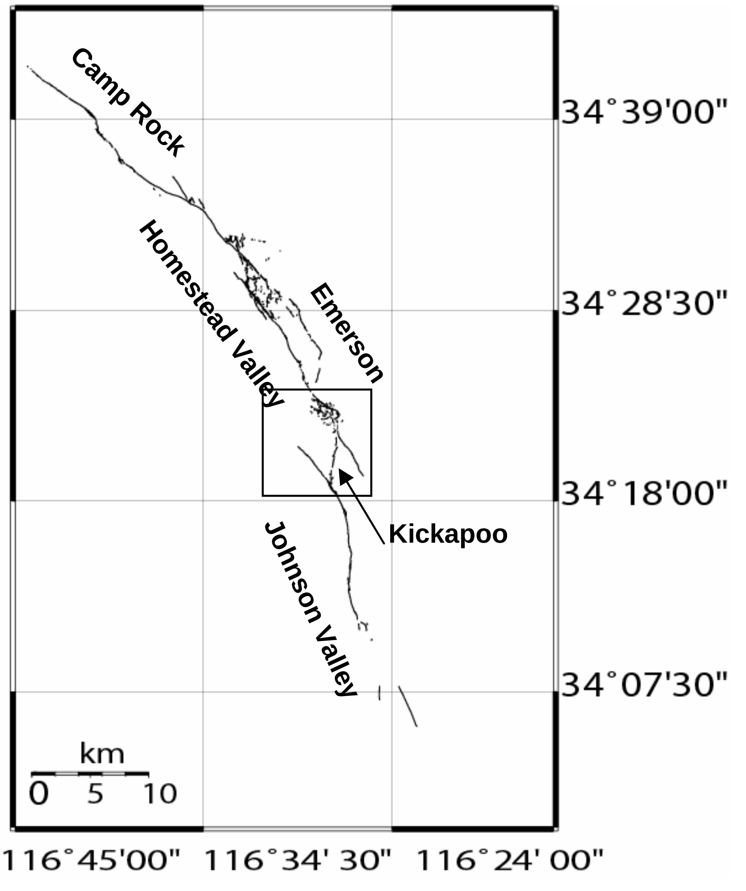

Figure 1, Michel and Avouac

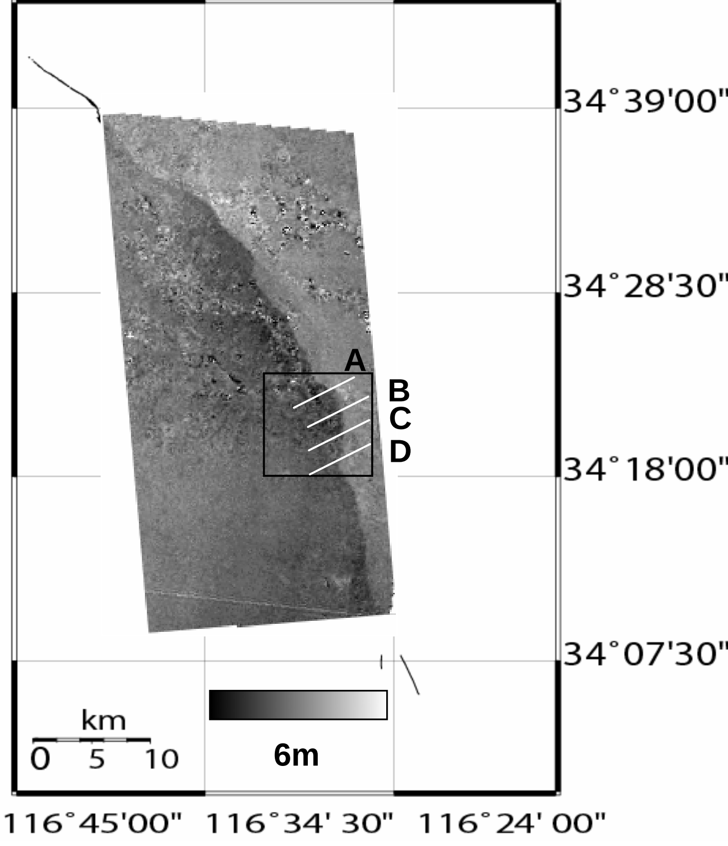

Figure 2, Michel and Avouac

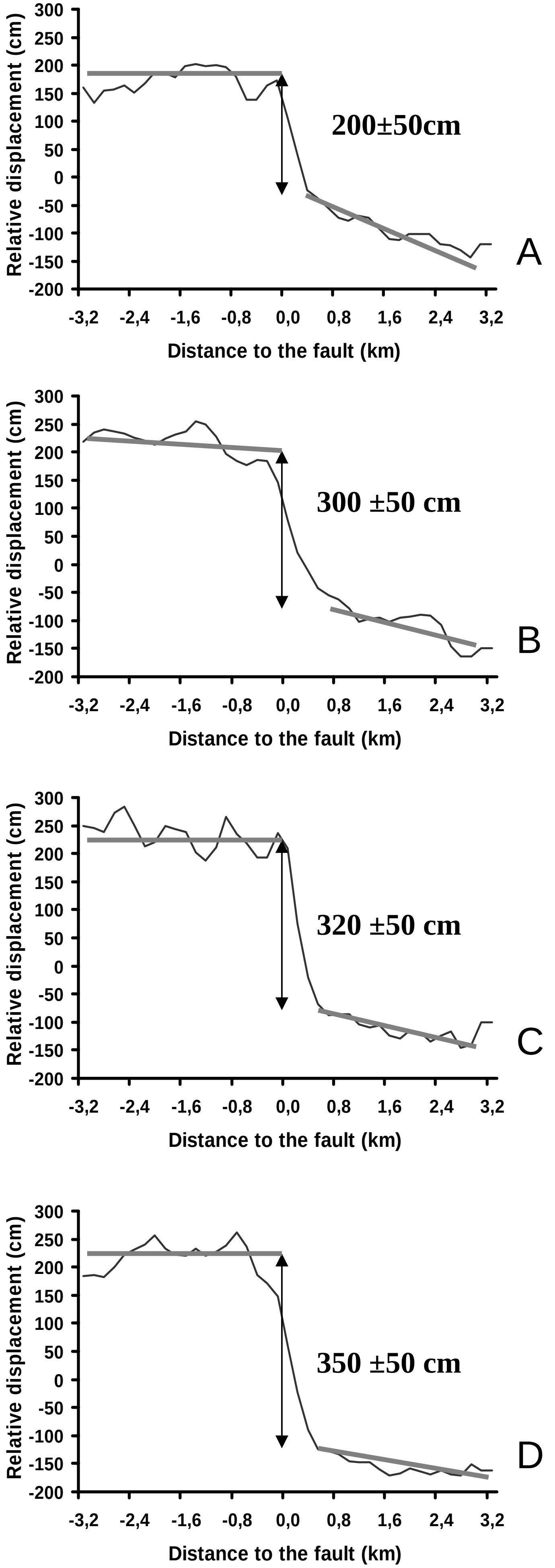

Figure 3, Michel and Avouac

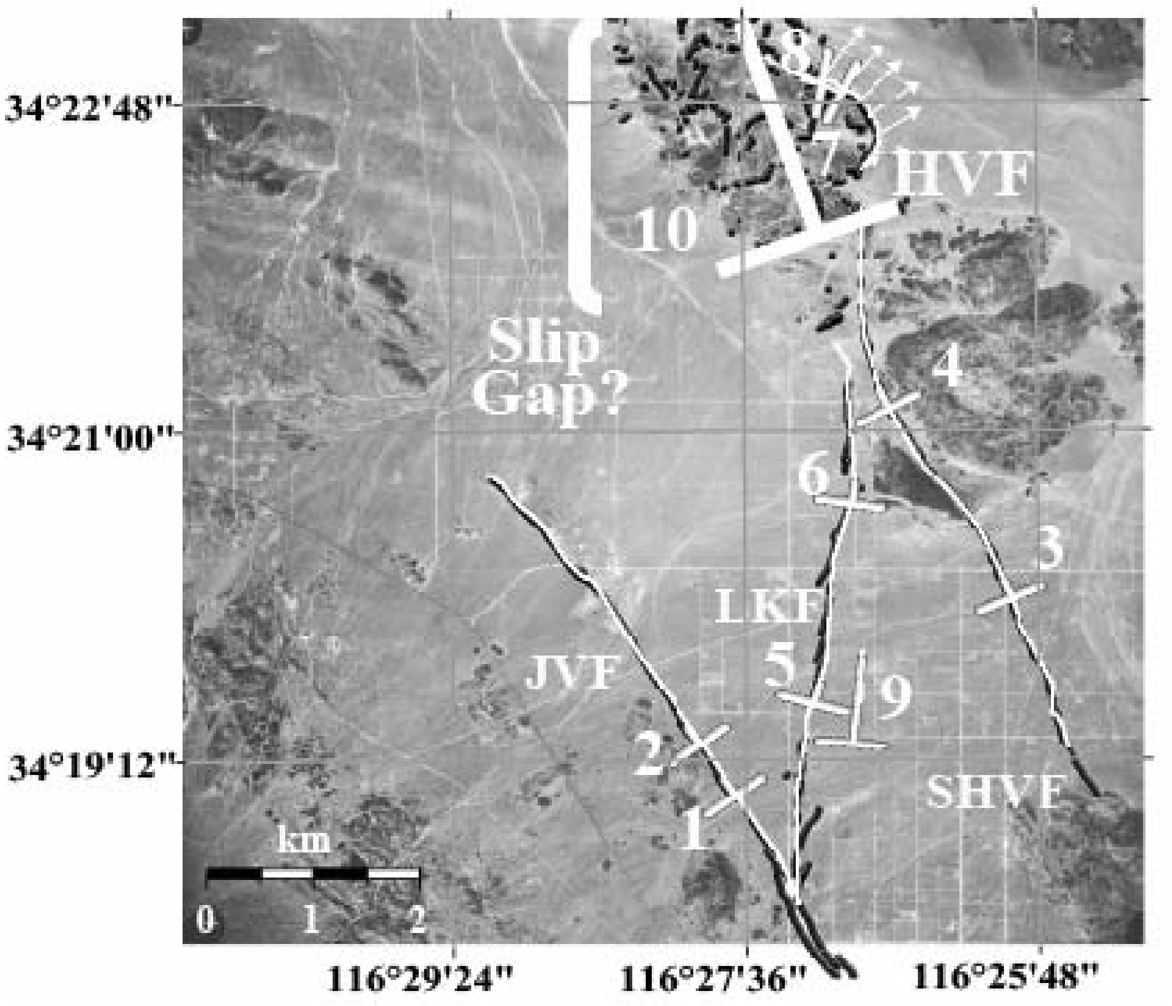

Figure 4, Michel and Avouac

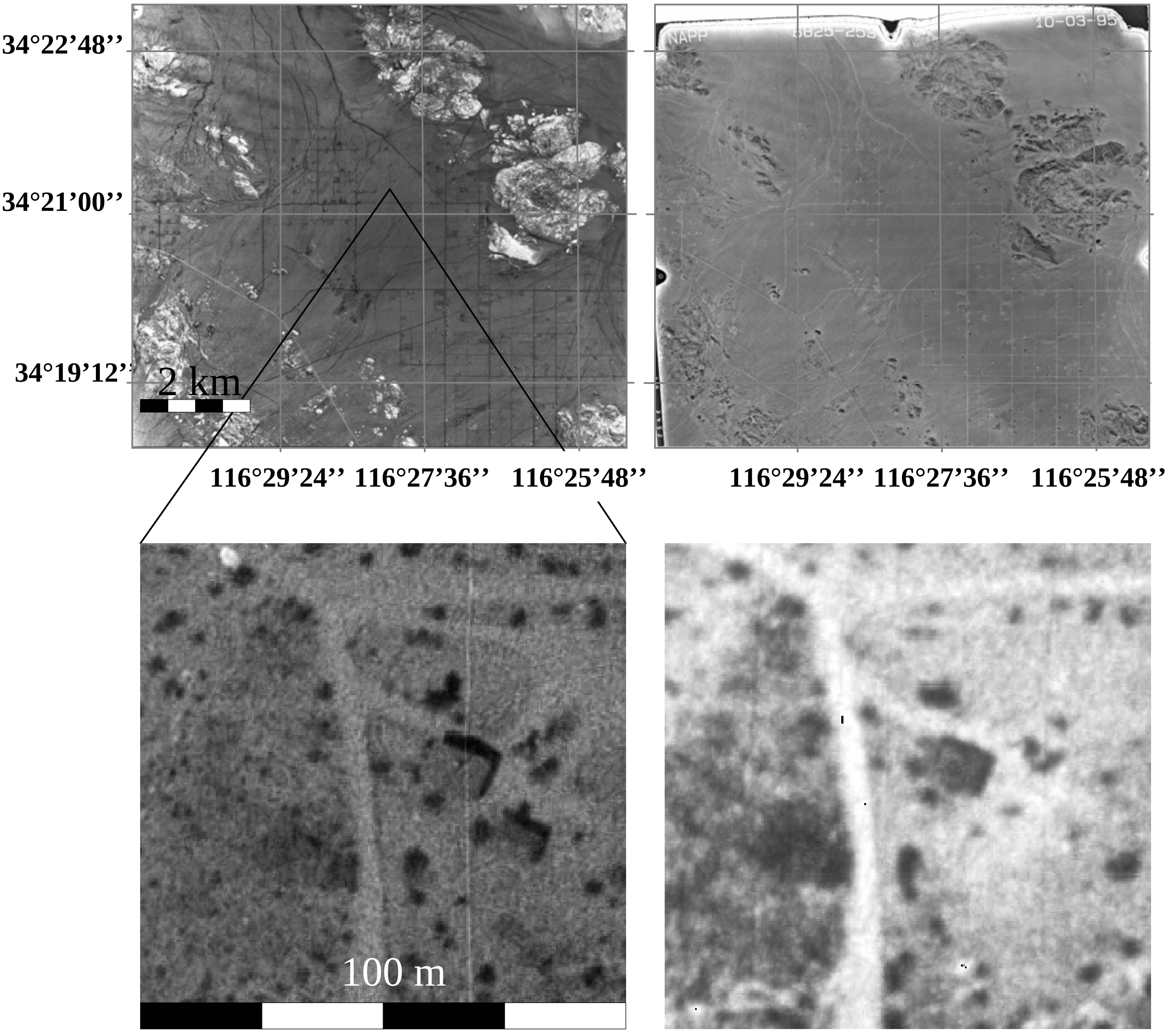

Figure 5, Michel and Avouac

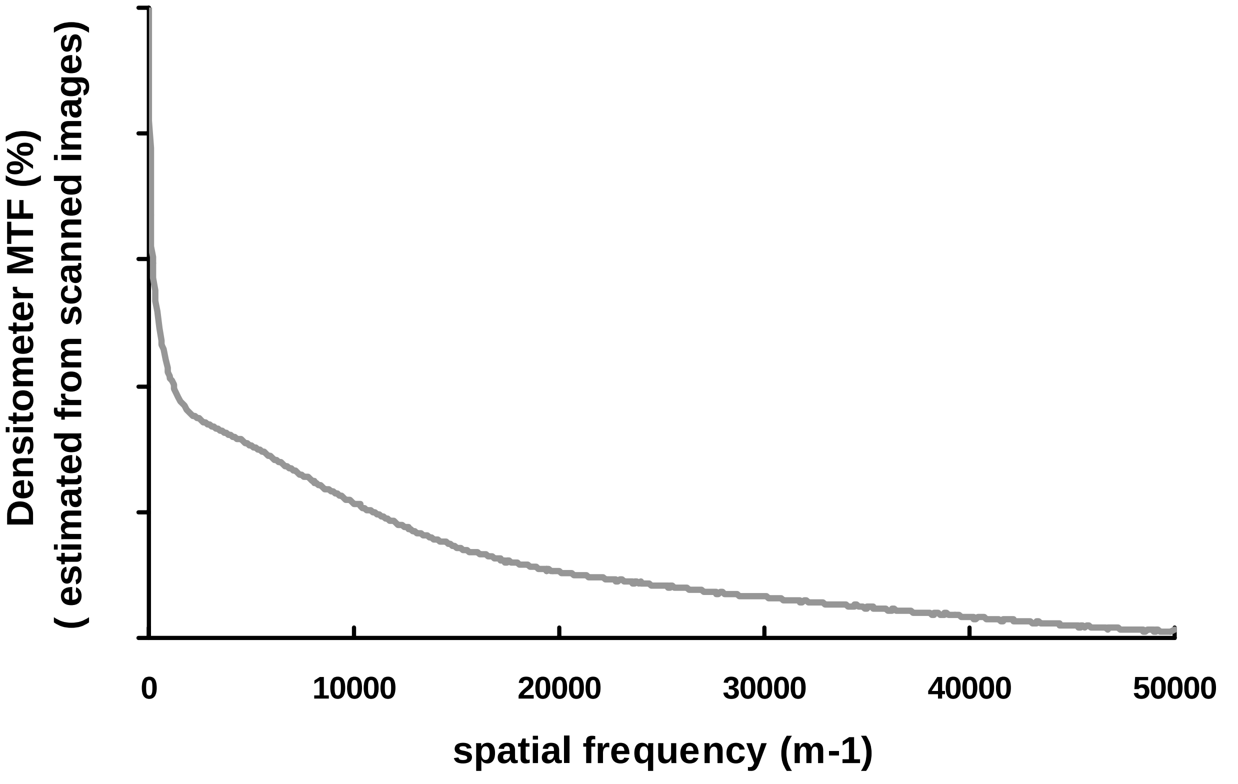

Figure 6, Michel and Avouac

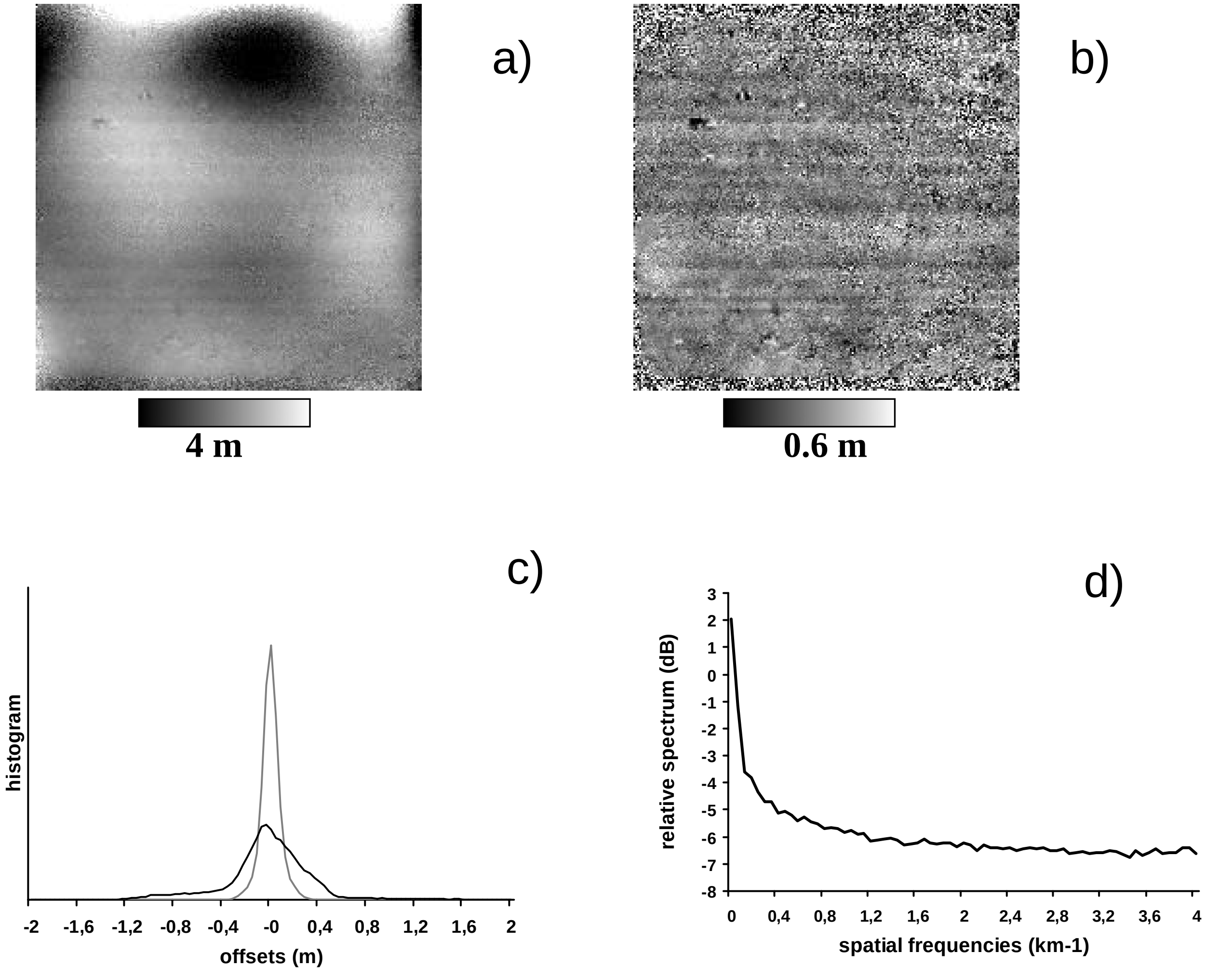

Figure 7, Michel and Avouac

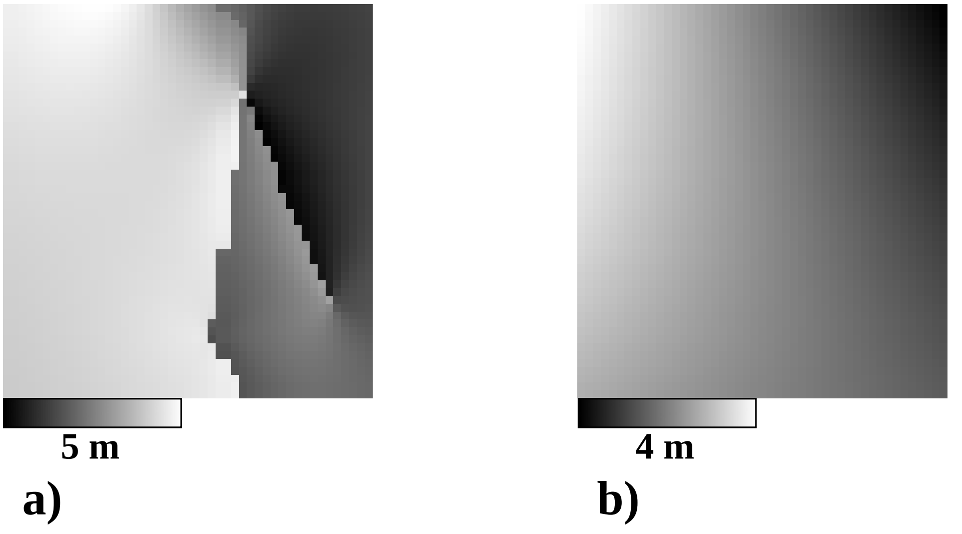

Figure 8, Michel and Avouac

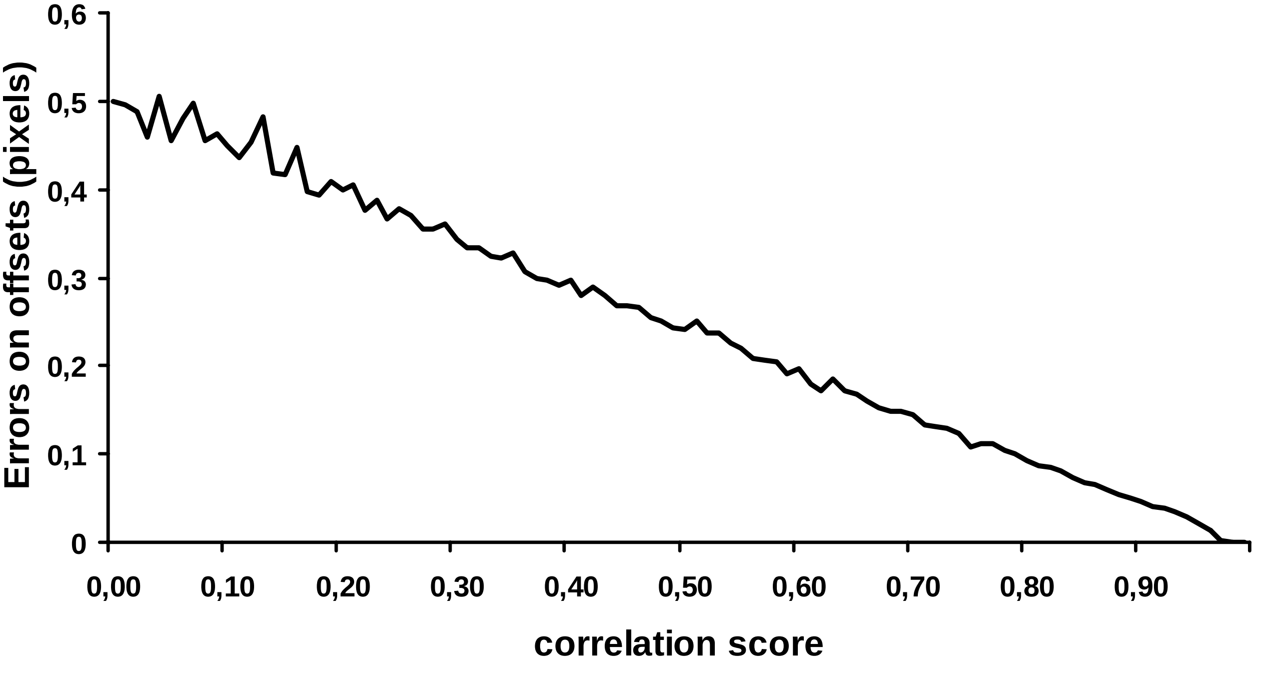

Figure 9, Michel and Avouac

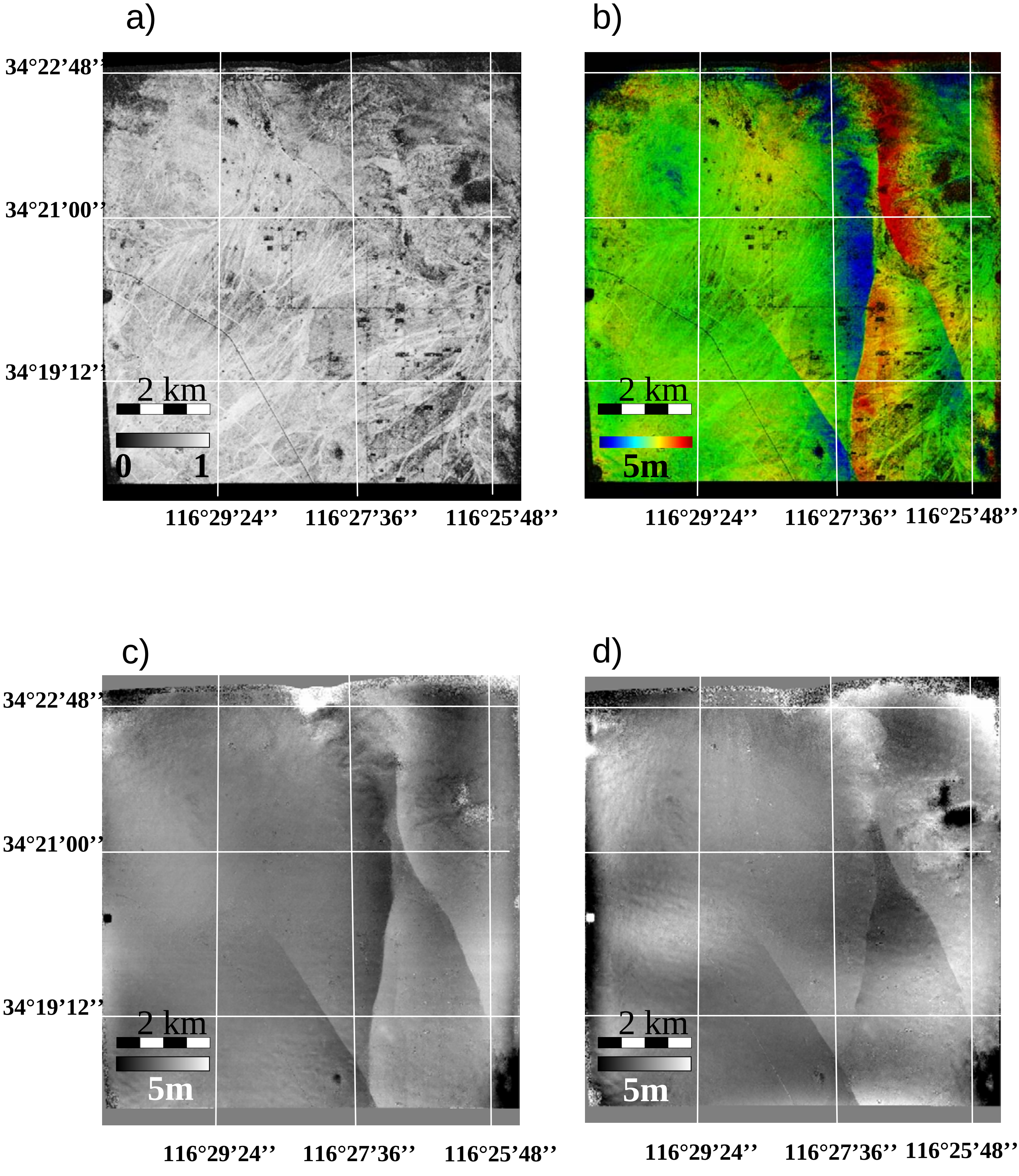

Figure 10, Michel and Avouac

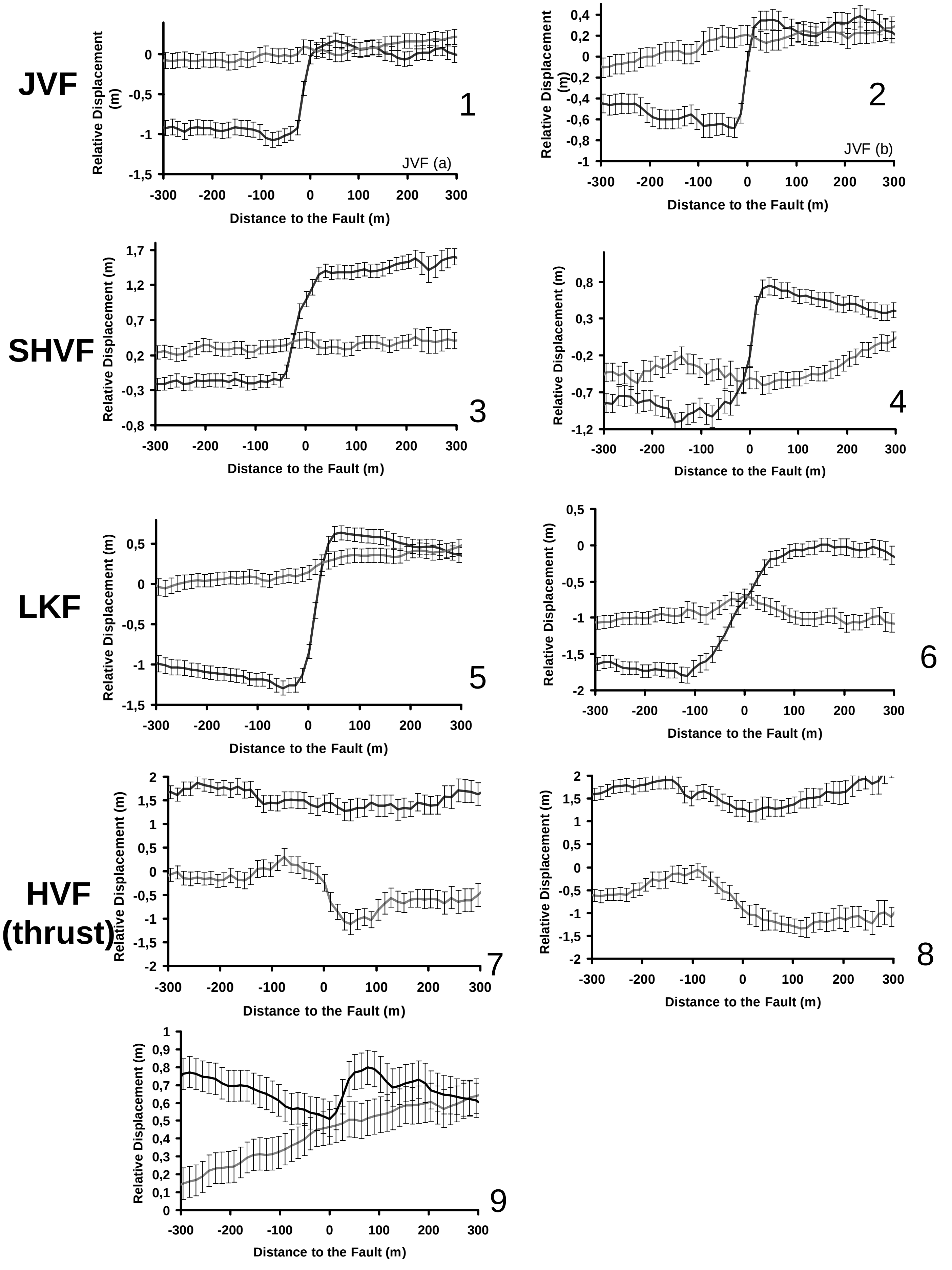

Figure 11, Michel and Avouac

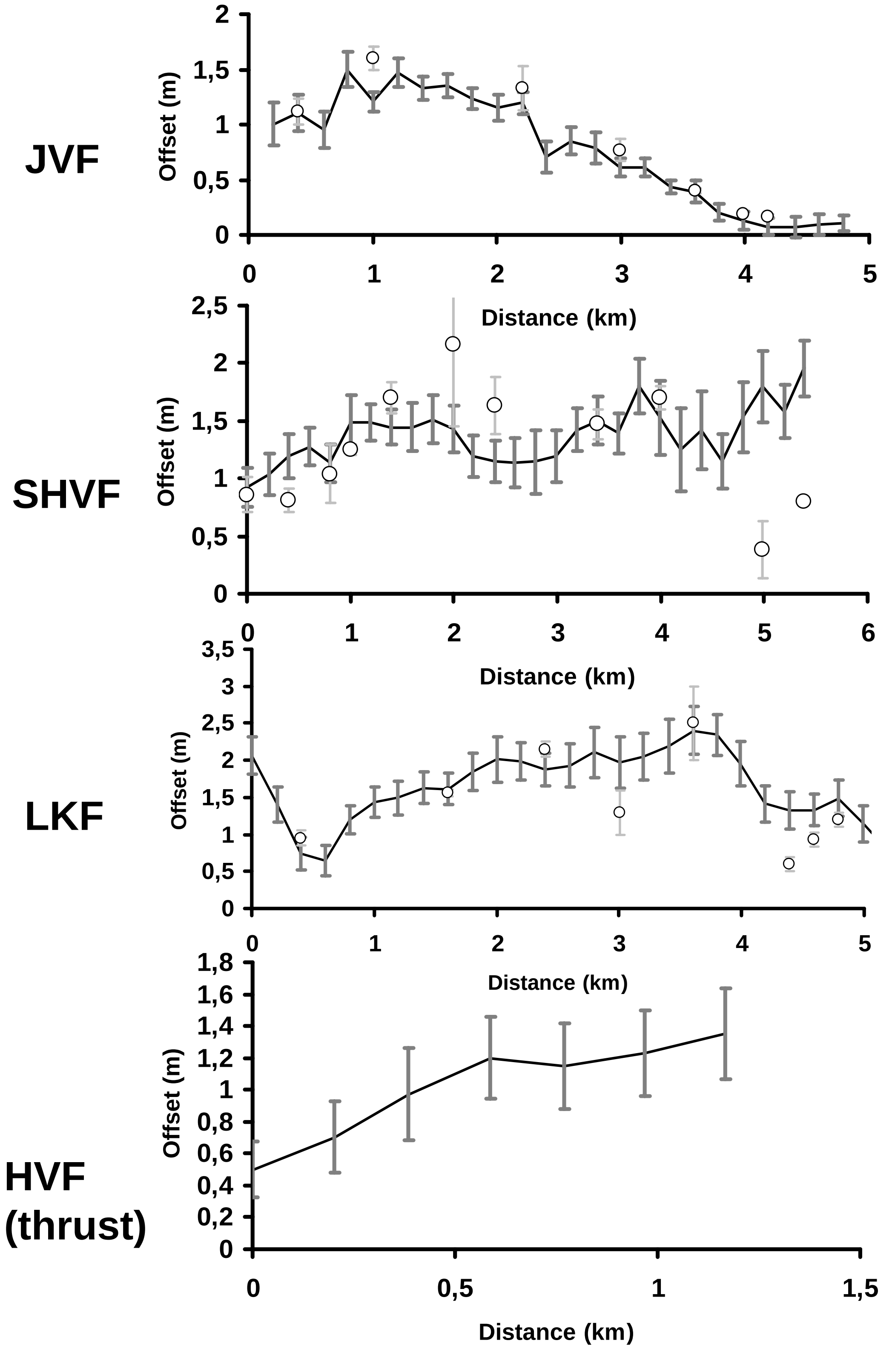

Figure 12, Michel and Avouac

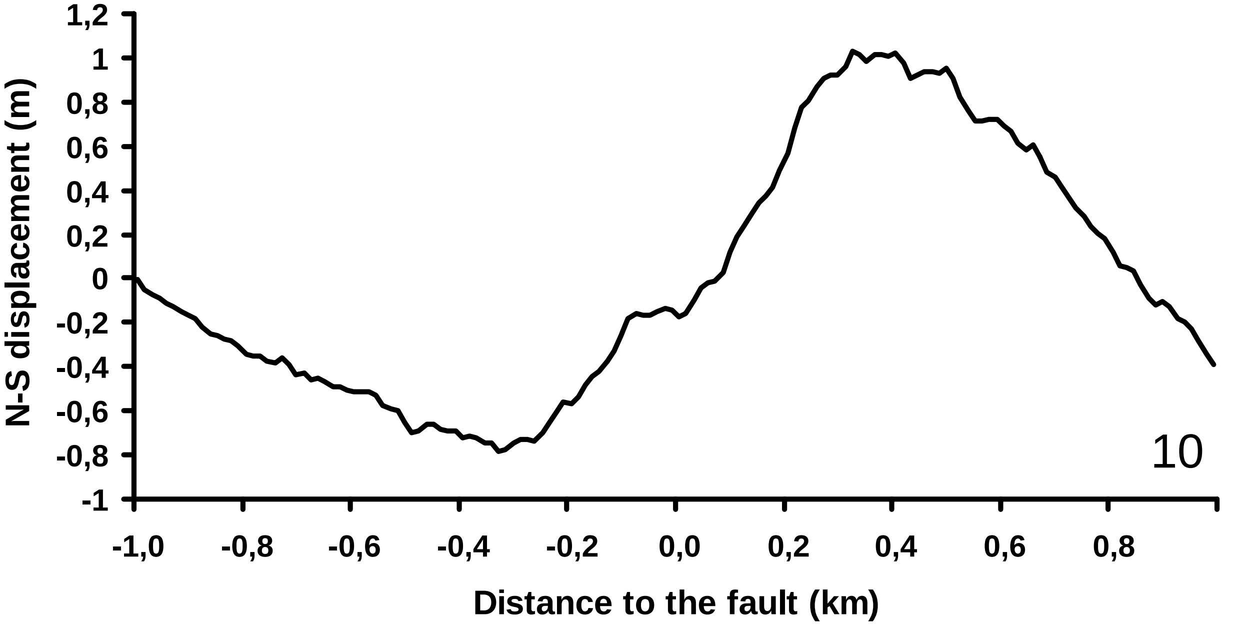

Figure 13, Michel and Avouac

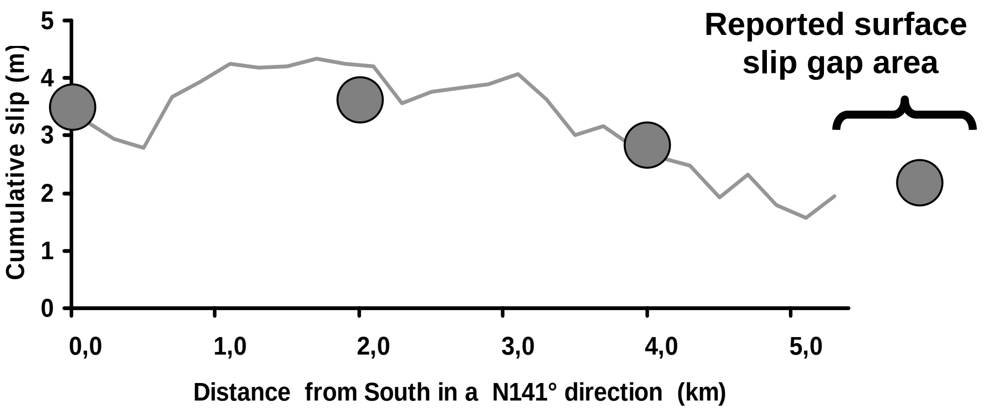

Figure 14, Michel and Avouac

Table 1 Data set

Material	Source	Reference	Characteristics
Images	US National Aerial Photography Program (NAPP)	Roll/frame, date (DD-MM-YYYY) Image 1: 1790-161, 25-07-1989 Image 2 6825-253, 10-03-1995 Image 3: 2498-144, 01-06-2002	Film negative 5 miles field of view about 1 m in ground resolution scene center coordinate : 34'20'38'N, 116'28'08'W
Digital Elevation Model	US National Elevation Dataset (NED)		3 arcsec in planimetric resolution about 10m (rms) in vertical accuracy
Microdensitometer	MAMA (Machine A Mesurer pour l'Astronomie, French national research equipment)	Not Applicable	12 bites digitation 10 µm in resolution 0.6 µm in accuracy 0.2 µm in repititivity

Table 2 error analysis

Source of error		Amplitude	Spatial frequency
Film	Thermo-Mechanical deformation	Several pixels	Low frequency (see Figure 7d)
Scan	Repetitivity and accuracy	Below 1/10th of the pixel size	High frequency Line oriented artifact
DEM	Uncertainty on elevation and planimetric resolution	Typically 10m (rms) for a 3 arsec resolution DEM,	Correlated to DEM errors
Correlation	Scene and snr dependant bias	About 1/10th of the pixel size	High frequency (offset map resolution)
Displacements of GCPs	Trade-off between viewing parameters and ground deformation	Several pixels	Low frequency polynomial